



A numerical simulation of pulverized coal combustion employing a tabulated-devolatilization-process model (TDP model)

Nozomu Hashimoto^{a,*}, Ryoichi Kurose^b, Seung-Min Hwang^c, Hirofumi Tsuji^a, Hiromi Shirai^a

^a Central Research Institute of Electric Power Industry (CRIEPI), 2-6-1 Nagasaka, Yokosuka 240-0196, Japan

^b Department of Mechanical Engineering and Science, Kyoto University, Kyoto 606-8501, Japan

^c Graduate School of Venture, Department of Health Environment, Hoseo University, 1463-10 Seocho 3dong, Seochogu, Seoul 137-867, Republic of Korea

ARTICLE INFO

Article history:

Received 14 February 2011

Received in revised form 30 May 2011

Accepted 30 May 2011

Available online 21 June 2011

Keywords:

Coal combustion
Numerical simulation
TDP model
Devolatilization
Particle heating rate

ABSTRACT

A new coal devolatilization model employing a tabulated-devolatilization-process model (TDP model) is developed, and its validity is investigated by performing a numerical simulation of a pulverized coal combustion field formed by an industrial low-NO_x burner in a 100 kg-coal/h test furnace. The predicted characteristics of the pulverized coal combustion field obtained from the simulation employing the TDP model are compared with those employing the conventional devolatilization model, those employing the two competing reaction rate model, and the experiments. The results show that drastic differences in the gas flow patterns and coal particle behavior appear between simulations. In particular, the recirculation flow behavior is strongly affected by the difference in the coal devolatilization model because of the difference in the volatile matter evolution rate. The TDP model captures the observed behavior of the coal particles in the experiment better than the other models. Although it is considered that by adjusting the devolatilization parameters the prediction similar to the TDP model is also possible by the other models, appropriate devolatilization parameters are automatically set to particles depending on the particle heating rate without trial-error method by employing the TDP model.

© 2011 The Combustion Institute. Published by Elsevier Inc. All rights reserved.

1. Introduction

Pulverized coal combustion is utilized in the majority of coal-fired thermal power plants. There are many types of problems in the operation of pulverized-coal-fired furnaces, e.g., fouling, slagging and sulfidation corrosion. The number of problems is expected to increase in the future owing to the increased use of low-grade coal, since world coal consumption will maintain an upward trend according to IEO2007 [2]. To solve such problems, understanding of the gas flow pattern, temperature distribution, gas species concentration distributions and coal particle behavior in the furnace is essential. In particular, the coal particle behavior in the burner region is important for the slagging and sulfidation corrosion problems because the accumulation of ash is directly affected by the particle behavior, and the local concentrations of corrosion-promoting substances such as H₂S are highly dependent on the coal particle behavior. Numerical simulations of a pulverized coal combustion field are effective for understanding such coal particle behavior in the furnace [3–7].

Recently, numerical simulations for large-scale pulverized-coal-fired furnaces have been performed by some researchers [8–16]. Since the numerical simulation of the pulverized coal combustion field is difficult because of the complexity of the coal combustion phenomena, comparatively simplified models for the devolatilization and combustion of coal particles are generally employed. However, sometimes employing such simplified models leads to relatively large errors in predicting the coal particle behavior in numerical simulations. One of the greatest simplifications of models employed for the numerical simulation of the pulverized coal combustion field is the devolatilization model.

It is well known that the devolatilization of coal particles is strongly affected by the coal particle heating rate [17,18]. Both the volatile matter evolution rate and the total amount of volatile matter evolved from a coal particle are generally enhanced by a high particle heating rate [19]. This fact has been reported by various researchers conducting experiments on the devolatilization of coal particles with more than one particle heating rate [20–24]. Nevertheless, most numerical simulations of the pulverized coal combustion field in large-scale furnaces employ a simplified model for the devolatilization of coal particles, in which the effect of the coal particle heating rate described above cannot be considered. In the simplified model (referred to as “the conventional model”, hereafter), the increase in the amount of volatile matter due to

* Corresponding author. Address: Energy Engineering Laboratory, Central Research Institute of Electric Power Industry (CRIEPI), 2-6-1 Nagasaka, Yokosuka 240-0196, Japan. Fax: +81 46 856 3346.

E-mail address: nozomu@criepi.denken.or.jp (N. Hashimoto).

Nomenclature

A_c	pre-exponential factor for Eq. (3.15), 1/s	Q	Q -factor
A_g	pre-exponential factor for Eq. (3.12), 1/s	q_{char}	heat gain due to the char combustion, J/s
A_p	projected area of particle, m^2	R	gas constant, J/(mol K)
A_s	surface area of particle, m^2	R_g	gaseous reaction rate regarding the kinetics, $\text{mol}/(\text{s m}^3)$
A_v	pre-exponential factor for the volatile matter evolution rate equation, Eq. (2.2), 1/s	T_g	gas temperature, K
$C_{p,p}$	specific heat of particle, J/(kg K)	T_p	particle temperature, K
$C_{p,g}$	specific heat of gas, J/(kg K)	u_{fi}	fluid velocity component for direction i , m/s
C	char mass, kg	u_{pi}	particle velocity component for direction i , m/s
D_p	particle diameter, m	U_X	mass fraction of chemical element X obtained by ultimate analysis (dry-ash-free basis), kg/kg-coal
E_c	activation energy for Eq. (3.15), J/kmol	U_z	mean axial particle velocity [m/s]
E_g	activation energy for Eq. (3.12), J/kmol	V	mass of volatile matter that has been evolved from a coal particle, kg
E_v	activation energy for the volatile matter evolution rate equation, Eq. (2.2), J/kmol	V^*	mass of volatile matter in particle, kg
GCV	calorific value of coal obtained by proximate analysis, J/kg-coal	X_i	molar fraction of chemical species i , mol/mol
h_X	enthalpy of chemical species X , J/kg	Y_i	mass fraction of chemical species i , kg/kg
k_g	thermal conductivity of gas, W/(m K)	$[X]$	molar concentration of chemical species X , mol/ m^3
K_v	devolatilization rate coefficient, 1/s		
K_i	reaction rate coefficient		
m_p	particle mass, kg		
$m_{p,w}$	moisture mass in particle, kg		
$m_{p,v}$	volatile matter mass in particle, kg		
m_{vola}	mass fraction of volatile matter in particle, kg/kg-coal		
m_X	mass fraction of chemical species X or chemical element X in a coal particle, kg/kg-coal		
M_X	molecular weight, kg/mol		
P_g	gas phase pressure, Pa		
P_X	mass fraction of substance X obtained by proximate analysis (as-received basis), kg/kg-coal		
Pr	Prandtl number		

Greek symbols

ε_p	absorptivity of coal particles
ρ_g	density of gas, kg/m^3
ρ_p	density of particle, kg/m^3
ν	kinematic viscosity of gas, m^2/s
σ	Stefan–Boltzmann constant
Δh_{char}	calorific value of char, J/kg
Δh_{dev}	required heat for devolatilization, 6.279×10^5 J/kg [1]
Δh_{lat}	latent heat of water, 2.254×10^6 J/kg
Δh_{vola}	calorific value of volatile matter, J/kg
Δh_{CH4low}	calorific value of CH_4 low, J/kg
$\Delta h_{\text{CH4high}}$	calorific value of CH_4 high, J/kg
Δh_{C2H2}	calorific value of C_2H_2 , J/kg

the high particle heating rate is considered by using Q -factor as following formula.

$$V^* = QV^{*f} \quad (1.1)$$

where V^* , V^{*f} and Q are the amount of volatile matter evolved from a coal particle in the numerical simulation, the amount of volatile matter obtained by the proximate analysis, and the Q -factor, respectively. The Q -factor is generally treated as a constant value for all coal particles regardless of the particle heating rate. In addition, the value of the Q -factor is based on empirical information obtained from different combustion fields, because an accurate value for the Q -factor cannot easily be obtained owing to the difficulty of estimating coal particle heating rate in the combustion field of interest before the execution of the numerical simulation.

Alternative model utilizing two competing mechanism was suggested by Kobayashi et al. [25] (two competing reaction rate model). In this model, the effect of coal particle heating rate on devolatilization of coal particle can be taken into account by considering the two competing overall reactions. However, it is difficult to obtain appropriate values for six parameters used in the model in advance of the simulation. Du and Chen [26] conducted numerical simulations of a coal combustion field using different sets of values for these parameters and found that these parameters strongly affect the simulation results. A trial-and-error method is required to obtain appropriate parameters for these parameters and it may take a lot of time and effort.

In this study, a new model for the devolatilization of coal particles referred to as the tabulated-devolatilization-process model (TDP model), in which appropriate values of the devolatilization parameters are selected for each coal particle from the

devolatilization database depending on the individual particle heating rate, is proposed. In addition, the validity of the TDP model is examined by performing numerical simulations employing the TDP model, the conventional model, and the two competing reaction rate model for a combustion field in a 100 kg-coal/h test furnace equipped with the $\text{Cl-}\alpha$ burner, which is a low- NO_x burner with the flame-stabilizing mechanism using a strong swirling flow. The predicted coal particle velocity in the test furnace is compared with the measurements using Laser Doppler velocimetry (LDV).

2. Modeling of the devolatilization of coal particles

2.1. Conventional model

In the numerical simulation of the pulverized coal combustion field, the following formula that was proposed by Badzioch and Hawksley [19] is commonly employed for modeling the devolatilization process:

$$\frac{dV}{dt} = K_v(V^* - V) \quad (2.1)$$

$$K_v = A_v \exp\left(-\frac{E_v}{RT_p}\right) \quad (2.2)$$

Here, V^* is expressed as

$$V^* = QV^{*f}, \quad (2.3)$$

where V^{*f} and Q are, respectively, the amount of volatile matter obtained by proximate analysis and the Q -factor, which is employed to consider the increase in the amount of volatile matter caused by the higher particle heating rate in a pulverized coal combustion field. In the conventional model for coal combustion, A_v , E_v and Q

are constant values for all coal particles regardless of the particle heating rate. However, the value of V^* strongly depends on the coal particle heating rate. Therefore, suitable values for A_v , E_v and Q vary considerably and depend on each particle diameter and how each particle is supplied to the coal combustion field. Such variation cannot be considered in the conventional model. In the next section, how suitable values for devolatilization parameters (A_v , E_v and Q) depend on the particle heating rate is examined.

In spite of many efforts by various researchers, the detailed chemical compounds in volatile matter are not completely understood because of the complexity of the chemical structure of coal. Therefore, the volatile matter is generally treated as a postulated substance in the numerical simulation of the coal combustion field. In the conventional model, the volatile matter is treated as the postulated substance, $C_aH_bO_c$, in which a , b and c represent the composition ratio of each chemical element. These composition ratios are calculated by the following equations.

$$a = \frac{(m_C)}{12} / \left(\frac{m_C}{12} + \frac{m_H}{1} + \frac{m_O}{16} \right) \quad (2.4)$$

$$b = \frac{(m_H)}{1} / \left(\frac{m_C}{12} + \frac{m_H}{1} + \frac{m_O}{16} \right) \quad (2.5)$$

$$c = \frac{(m_O)}{16} / \left(\frac{m_C}{12} + \frac{m_H}{1} + \frac{m_O}{16} \right) \quad (2.6)$$

$$m_C = 1 - (U_O + U_H) / \left(\frac{P_{\text{vola}} \times Q}{P_{\text{vola}} + P_{\text{fixC}}} \right) \quad (2.7)$$

$$m_H = U_H / \left(\frac{P_{\text{vola}} \times Q}{P_{\text{vola}} + P_{\text{fixC}}} \right) \quad (2.8)$$

$$m_O = U_O / \left(\frac{P_{\text{vola}} \times Q}{P_{\text{vola}} + P_{\text{fixC}}} \right) \quad (2.9)$$

The overall reaction of $C_aH_bO_c$ is expressed as



where α , β and γ can be calculated from the values of a , b and c . As previously mentioned, the detailed chemical species in the volatile matter are not completely understood. However, the overall calorific value of the coal, which is the sum of the calorific values of the volatile matter and the char, can be known by proximate analysis. The overall calorific value in the numerical simulation should correspond to the calorific value of the coal obtained from proximate analysis because the overall calorific value is constant, regardless of the pathway taken to achieve the products, as stated by the well-known Hess's law. The calorific value of $C_aH_bO_c$ is calculated by the following equation.

$$\Delta h_{\text{vola}} = \frac{GCV - \Delta h_{\text{char}} m_{C,\text{char}} + \Delta h_{\text{lat}} P_{\text{moist}}}{m_{\text{vola}}} + \Delta h_{\text{dev}} \quad (2.11)$$

$$\Delta h_{\text{char}} = h_C + \frac{M_{O_2}}{M_C} h_{O_2} - \frac{M_{CO_2}}{M_C} h_{CO_2} \quad (2.12)$$

Here, the calorific value of the char, Δh_{char} , is regarded to be equal to that of the fixed carbon. Using these equations, the overall calorific value of a coal particle (MJ/kg-coal) in the numerical simulation can be conformed to the calorific value of coal obtained from proximate analysis.

2.2. Effects of coal particle heating rate on devolatilization characteristics

To investigate the effects of the coal particle heating rate on A_v , E_v and V^*/V^{**} , the devolatilization simulations were performed for some coal rank. Properties of coals for the devolatilization simulations are listed in Table 1. In Table 1, the fuel ratio is defined as the volatile matter mass fraction divided by the fixed carbon mass fraction. A number of devolatilization models have been developed by various researchers, such as the CPD model [28,29], FG-DVC

Table 1
Coal properties for devolatilization simulation.

Coal	Newlands	Wambo	Plateau	Adaro
<i>Proximate analysis (wt.%)</i>				
Moisture ^a	2.5	3.5	5.9	21.9
Volatile matter ^b	28.4	35.7	41.3	54.7
Fixed carbon ^b	56.4	54.6	48.8	44.0
Ash ^b	15.2	9.7	9.9	1.3
Fuel ratio (-)	1.97	1.53	1.18	0.80
<i>Ultimate analysis^b (wt.%)</i>				
C	71.8	74.2	71.9	72.5
H	4.5	5.6	5.5	6.2
N	1.6	1.8	1.3	0.9
O	6.4	8.3	11.1	19.1
Combustible sulfur	0.5	0.4	0.4	0.1
Heating value (low) ^b (MJ/kg)	28.2	29.6	28.8	29.6

^a As received basis.

^b Dry basis.

model [30] and FLASHCHAIN model [31–38]. In this study, the FLASHCHAIN model and the CPD model, which can predict the detailed devolatilization process of coal particles, are used for the devolatilization simulations. For the FLASHCHAIN model, only the data from proximate analysis and ultimate analysis are required, while four of the parameters from ¹³C NMR measurement, which are M_{cl} (the average molecular weight per aromatic cluster), M_{δ} (the average side-chain molecular weight), $\sigma + 1$ (the average number of attachments per cluster), and p_0 (the fraction of intact bridges), in addition to the data from ultimate analysis are required for the CPD model. Since the data from ¹³C NMR measurement were not available, these four parameters for the CPD model were estimated by the correlation proposed by Genetti et al. [39].

Figures 1 and 2 show V^*/V^{**} , which is appropriate value for the Q -factor, as a function of coal particle heating rate for different coal rank. For the CPD model, the result for Adaro coal could not be obtained because of the divergence in the simulation. This is considered to be caused by that the properties of Adaro was out of range for the correlation. It is shown that V^*/V^{**} increases with increasing coal particle heating rate for all coal rank in both Figs. 1 and 2. It is found that the variation of V^*/V^{**} with the coal particle heating rate is large. In Fig. 1 (predicted by the FLASHCHAIN model), for instance, when the coal particle heating rate increases from 3×10^3 to 2×10^5 K/s, V^*/V^{**} increases from 1.4 to 1.7 for Newlands, a change of more than 20%. In the same way, V^*/V^{**} increases from 1.42 to 1.54, which is more than 8%, with the increase of the heating rate from 10^3 to 10^6 K/s for Newlands, in Fig. 2 (predicted by the CPD model).

Figures 3 and 4 show the effect of the coal particle heating rate on the devolatilization rate coefficient, K_v , for Newlands coal predicted by the FLASHCHAIN model and the CPD model in an

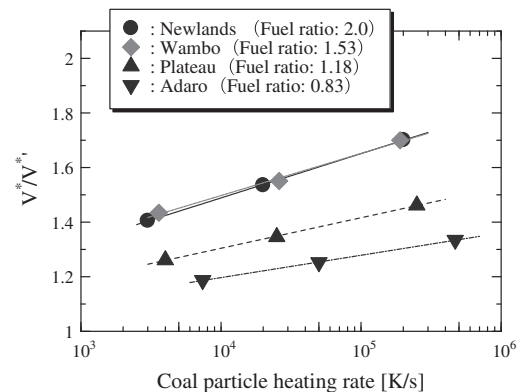


Fig. 1. V^*/V^{**} (Appropriate value for Q -factor) as a function of the coal particle heating rate calculated by the FLASHCHAIN model.

Arrhenius diagrams. It is found that K_v increases with the increase of heating rate for both the FLASHCHAIN model and the CPD model. In Fig. 3 (predicted by the FLASHCHAIN model), for example, K_v increases by approximately two orders of magnitude when the coal particle heating rate increases from 3×10^3 to 2×10^5 K/s. In the same manner, K_v increases over two orders of magnitude when the coal particle heating rate increases from 10^3 to 10^6 K/s, in Fig. 4 (predicted by the CPD model). Although there are some discrepancies between absolute values predicted by the FLASHCHAIN model and that predicted by the CPD model, the tendencies that the K_v increases with the heating rate monotonically are consistent.

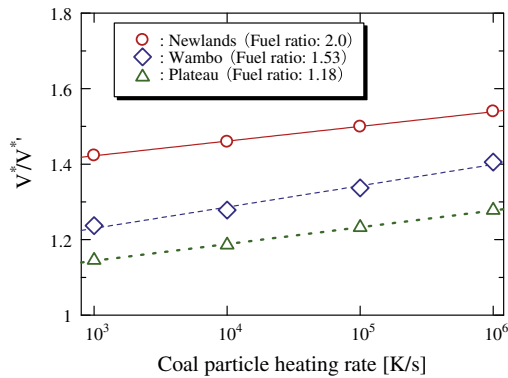


Fig. 2. V^*/V'' (Appropriate value for Q -factor) as a function of the coal particle heating rate calculated by the CPD model.

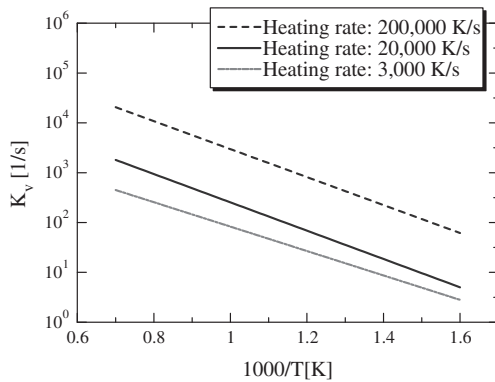


Fig. 3. Effect of the coal particle heating rate on K_v (in Eq. (2.1)) for Newlands coal calculated by the FLASHCHAIN model.

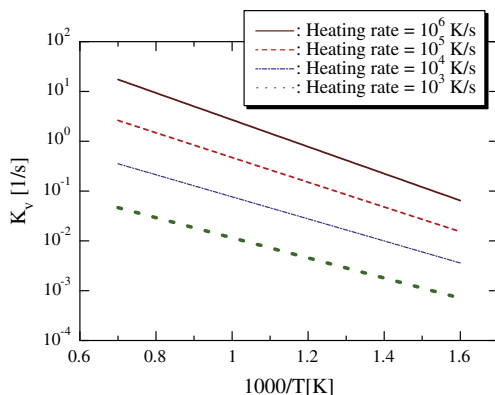
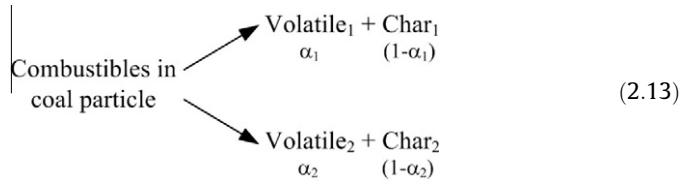


Fig. 4. Effect of the coal particle heating rate on K_v (in Eq. (2.1)) for Newlands coal calculated by the CPD model.

Despite the fact that there are large variations of appropriate values for the devolatilization parameters depending on the coal particle heating rate, the devolatilization parameters are identical for all coal particles in the conventional model. Such a treatment can cause relatively large errors in the predicted amount of the volatile matter evolved from coal particles in a numerical simulation. These errors can cause errors in the prediction of gas flows and particle behavior. To minimize such errors, a new model for the devolatilization is developed in this study.

2.3. Two competing rate reaction model

To take into account the effects of heating rate on devolatilization parameters, the model utilizing two competing mechanism was suggested by Kobayashi et al. [25] (two competing reaction rate model). In this model, two competing overall reactions are considered as follows.



The volatile evolution rate is expressed by following equations.

$$\frac{V(t)}{(1 - P_{\text{moist}} - P_{\text{ash}})m_p} = \int_0^t (\alpha_1 R_1 + \alpha_2 R_2) \exp\left(-\int_0^t (R_1 + R_2) dt\right) dt \quad (2.14)$$

$$R_1 = A_1 \exp\left(-\frac{E_1}{RT_p}\right) \quad (2.15)$$

$$R_2 = A_2 \exp\left(-\frac{E_2}{RT_p}\right) \quad (2.16)$$

Here, α_1 and α_2 are mass stoichiometric coefficients, A_1 and A_2 are pre-exponential factors, E_1 and E_2 are activation energies for two reactions. Using this model, the changes in the amount of volatile matter and devolatilization rate depending on particle heating rate can be considered. However, it is difficult to obtain appropriate values for these six parameters in advance of the simulation. Du and Chen [26] conducted numerical simulations of a coal combustion field using different sets of values for these parameters and found that these parameters strongly affect the simulation results. A trial-and-error method is required to obtain appropriate parameters for these parameters and it may take a lot of time and effort.

2.4. Tabulated-devolatilization-process model (TDP model)

To consider the variation of A_v , E_v and m_{vola} for each coal particle, a new model employing a tabulated-devolatilization-process model (TDP model) is developed in this study. Figure 5 shows calculation flow charts for the conventional model and TDP model. In the TDP model, a devolatilization database including various temperature histories and devolatilization parameters (A_v , E_v and m_{vola}) for each temperature history is prepared in advance of the calculation. The devolatilization database can be constructed from the results of experiments using apparatus such as a drop tube furnace as well as from the results of simulations using devolatilization models such as the CPD model [28,29], FG-DVC model [30] or FLASHCHAIN model [31–38]. In this study, PC Coal Lab [40], which can simulate the devolatilization process of a coal particle based on the FLASHCHAIN model [31–38], was used to produce the devolatilization database. The number of temperature histories in the database produced using PC Coal Lab is 81, with

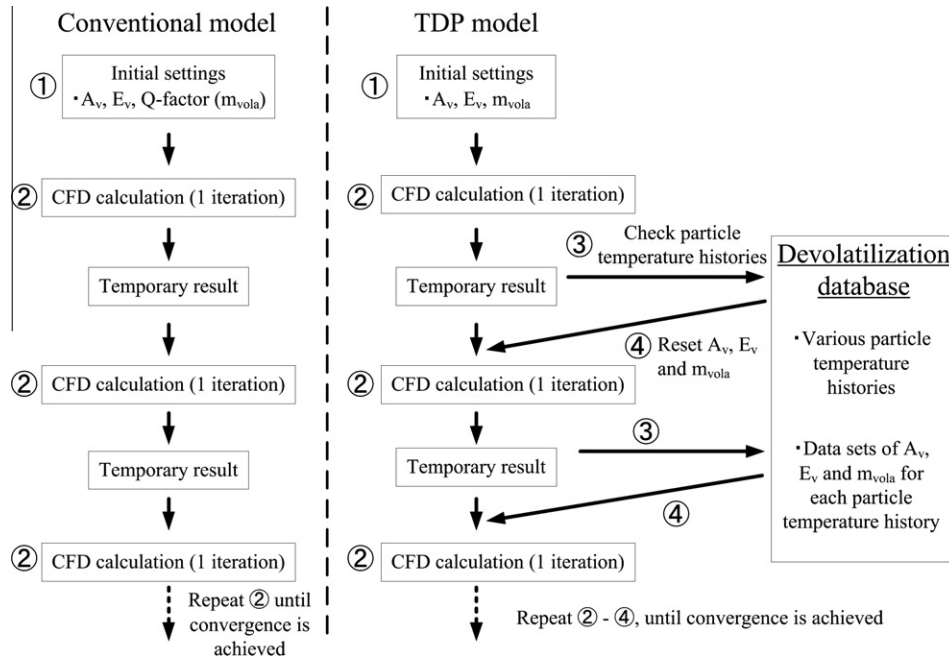


Fig. 5. Calculation flow charts for the conventional model and TDP model.

particle heating rates of 1.7×10^3 – 5.9×10^7 K/s. In the conventional model, the devolatilization parameters are unchanged during the CFD calculation as shown in Fig. 5. In the TDP model, on the other hand, appropriate values for the devolatilization parameters are set for each coal particle at each iteration step. The concrete procedure is as follows:

1. First, the devolatilization parameters are set at initial values.
2. The CFD calculation is performed using the devolatilization parameters.
3. After one iteration, the particle temperature history calculated in the last iteration is compared with all temperature histories in the devolatilization database for each coal particle (Fig. 6). The temperature history that is closest to the particle temperature history obtained from the last CFD iteration is selected from the devolatilization database.
4. The devolatilization parameters associated with the selected temperature history are set as the parameters for the next CFD iteration.

Steps 2–4 are repeated until the convergence of the CFD calculation result is achieved.

In the TDP model, m_{vola} varies with the particle heating rate as previously explained. The variation of m_{vola} means the variation of the chemical elements composition ratio and the calorific value of

the volatile matter. Therefore, a number of the volatile matters as postulated chemical species must be defined if the volatile matters are to be treated in the same manner as in the conventional model, i.e., treating the volatile matters as $C_aH_bO_c$. In this case, a large computation time is required because a number of transport equations for $C_aH_bO_c$ must be solved. In the TDP model, to avoid a large increase in the computation time, the volatile matters are treated as postulated chemical species composed of $CH_{4\text{low}}$, $CH_{4\text{high}}$, C_2H_2 , O_2 and H_{CN} , instead of $C_aH_bO_c$ as in the conventional model. $CH_{4\text{low}}$ and $CH_{4\text{high}}$ have same composition of chemical elements but their calorific values are different. By employing this treatment of the volatile matter, the number of chemical species that must be defined is not changed even if the number of values for m_{vola} is increased by the addition of data to the devolatilization database. The mass fractions of the chemical species are expressed by the following equations.

$$m_{\text{vola}} = m_{\text{CH}_4} + m_{\text{C}_2\text{H}_2} + m_{\text{O}_2} + m_{\text{HCN}} \quad (2.17)$$

$$m_{\text{vola}} = m_{\text{C,vola}} + m_{\text{H}} + m_{\text{O}} + (1 - \kappa)m_{\text{N}} \quad (2.18)$$

$$m_{\text{C,vola}} = \frac{12}{16}m_{\text{CH}_4} + \frac{24}{26}m_{\text{C}_2\text{H}_2} + \frac{12}{27}m_{\text{HCN}} \quad (2.19)$$

$$m_{\text{C,char}} = (1 - P_{\text{moist}} - P_{\text{ash}}) \times U_{\text{C}} - m_{\text{C,vola}} \quad (2.20)$$

$$\begin{aligned} m_{\text{H}} &= (1 - P_{\text{moist}} - P_{\text{ash}}) \times U_{\text{H}} \\ &= \frac{4}{16}m_{\text{CH}_4} + \frac{2}{26}m_{\text{C}_2\text{H}_2} + \frac{1}{27}m_{\text{HCN}} \end{aligned} \quad (2.21)$$

$$m_{\text{O}} = (1 - P_{\text{moist}} - P_{\text{ash}}) \times U_{\text{O}} = m_{\text{O}_2} \quad (2.22)$$

$$m_{\text{N}} = (1 - P_{\text{moist}} - P_{\text{ash}}) \times U_{\text{N}} = \frac{1}{(1 - \kappa)} \frac{14}{27}m_{\text{HCN}} \quad (2.23)$$

$$m_{\text{C,char}} + m_{\text{vola}} = (1 - P_{\text{moist}} - P_{\text{ash}}) \quad (2.24)$$

The mass fraction of each chemical species for an arbitrary value of m_{vola} can be obtained by solving the above simultaneous equations.

To conform the overall calorific value of a coal particle in the numerical simulation to the calorific value obtained by proximate analysis, the ratio of the mass fraction between $CH_{4\text{low}}$ and $CH_{4\text{high}}$ is calculated by the following equations.

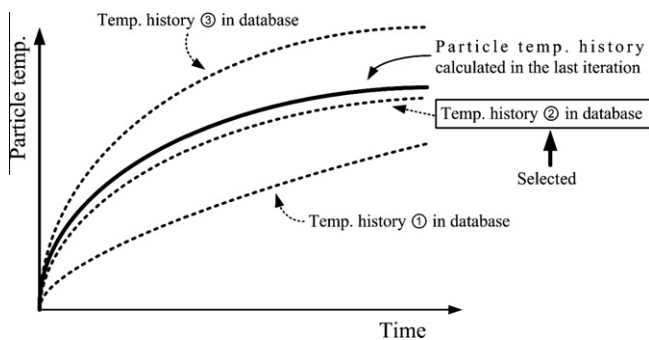


Fig. 6. Schematic diagram of selection process (step 3 in Fig. 5).

$$\Delta h_{\text{vola}} = \frac{m_{\text{CH4}}}{m_{\text{vola}}} (\xi \Delta h_{\text{CH4low}} + (1 - \xi) \Delta h_{\text{CH4high}}) + \frac{m_{\text{C2H2}}}{m_{\text{vola}}} \Delta h_{\text{C2H2}} \quad (2.25)$$

$$\Delta h_{\text{vola}} = \frac{\text{GCV} - \Delta h_{\text{char}} m_{\text{C, char}} + \Delta h_{\text{lat}} P_{\text{moist}}}{m_{\text{vola}}} + \Delta h_{\text{dev}} \quad (2.26)$$

$$\Delta h_{\text{char}} = h_{\text{C}} + \frac{M_{\text{O2}}}{M_{\text{C}}} h_{\text{O2}} - \frac{M_{\text{CO2}}}{M_{\text{C}}} h_{\text{CO2}} \quad (2.27)$$

$$m_{\text{CH4}} = \xi m_{\text{CH4low}} + (1 - \xi) m_{\text{CH4high}} \quad (2.28)$$

Using the Eqs. (2.25)–(2.28), the overall calorific value of a coal particle (MJ/kg-coal) in the numerical simulation employing the TDP model can be conformed to the calorific value of the coal obtained from proximate analysis, same as the conventional model.

3. Other models for numerical simulations of pulverized coal combustion field

The simulation was performed using the STAR-CD code with the TDP model incorporated as a user subroutine. The mathematical models and numerical methods other than the devolatilization model employed here are as follows.

The gas-phase turbulence was represented by the renormalization group (RNG) k - ε model [41,42], which is believed to give more accurate results for swirling and other highly strained flows than the generally used standard k - ε model [43]. The gas-phase time-averaged continuity equation and conservation equations of the momentum, turbulent kinetic energy, dissipation, enthalpy and species are

$$\frac{\partial}{\partial x_i} (\rho_g u_i) = 0 \quad (3.1)$$

$$\frac{\partial}{\partial x_i} (\rho_g u_i \phi) = \frac{\partial}{\partial x_i} \left(\Gamma_\phi \frac{\partial \phi}{\partial x_i} \right) + S_\phi + S_{p\phi}, \quad (3.2)$$

where ϕ denotes the generalized variables expressing fluid velocity components u_i , the turbulent kinetic energy k , the rate of eddy dissipation ε , the fluid enthalpy h and the mass fractions of chemical species Y_i . Γ_ϕ denotes the turbulent exchange coefficient, and S_f and $S_{p\phi}$ represent the gas-phase source terms that are in addition to the convection and diffusion terms and the particle-phase source terms, respectively. The actual forms of these terms are provided in other papers [41–44]. The continuity and momentum equations were solved using the PISO algorithm [45,46]. The nonlinear terms in the conservation equations were approximated by a first-order upwind scheme, and a second-order central-difference scheme was employed for other derivatives.

The equation of motion for the representative coal particles is given by

$$m_p \frac{du_{pi}}{dt} = \frac{1}{2} C_d \rho_p A_p |u_{fi} - u_{pi}| (u_{fi} - u_{pi}) \quad (3.3)$$

$$C_d = \frac{24(1 + 0.15 \text{Re}_p^{0.687})}{\text{Re}_p} \quad (3.4)$$

$$\text{Re}_p = \frac{D_p |u_{fi} - u_{pi}|}{\nu} \quad (3.5)$$

The effect of the turbulence of the gas phase on particle motion was modeled by a stochastic method [47]. The particle temperature T_p was calculated by considering the heat transfer due to convection, radiation, heat loss due to the evaporation of moisture and the devolatilization reaction in coal particle, and heat gain due to char combustion, using the following equation:

$$m_p c_{p,p} \frac{dT_p}{dt} = -A_s h (T_p - T_g) + A_s \varepsilon_p \sigma (\Theta_R^4 - T_p^4) + \Delta h_{\text{lat}} \frac{dm_{p,w}}{dt} + \Delta h_{\text{dev}} \frac{dm_{p,v}}{dt} + \dot{q}_{\text{char}} \quad (3.6)$$

$$h = \frac{k_g Z (2 + 0.6 \text{Re}_p^{1/2} \text{Pr}^{1/3})}{(e^Z - 1) D_p} \quad (3.7)$$

$$Z = \frac{-c_{p,g} (dm_p/dt)}{\pi D_p k_g (2 + 0.6 \text{Re}_p^{1/2} \text{Pr}^{1/3})} \quad (3.8)$$

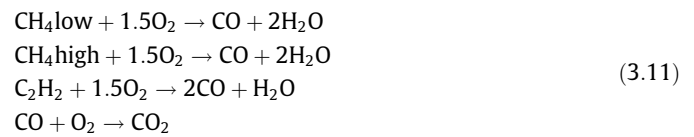
$$\Theta_R = (I/4\sigma)^{1/4}, \quad (3.9)$$

where the radiant intensity I [$\text{J}/(\text{m}^2 \text{s})$] was calculated by the discrete ordinates method [48], which simulates the radiative heat transfer among the gas, particles and wall. The absorptivities of the coal particles and wall are assumed to be 0.85 and 0.4, respectively. Also, the absorption coefficient of the gas was set at 0.075. The interaction of the conserved properties between the gas phase and the coal particles was calculated by the particle-source-in cell (PSI-Cell) technique [49].

Gaseous combustion between the volatile matter and air was calculated using a combined model of the kinetics and eddy dissipation models [50]. The chemical mechanism consists of two global reactions. In the conventional model, the reactions are expressed by the following formulas.



In the TDP model, the reactions are expressed by the following formulas:



Regarding the kinetics, the rate of reaction for the reactants is given as an Arrhenius expression:

$$R_g = A_g T_g^d \exp\left(-\frac{E_g}{RT_g}\right) [\text{Reactant}]^f [\text{H}_2\text{O}]^h [\text{O}_2]^k. \quad (3.12)$$

In this study, the rate parameters for 2-step global reaction of CH_4 employed by Pember et al. [51] are used as the rate parameters for all of reactions of volatile matter. The parameters in Eqs. (5.6) and (5.8) in Ref. [51] are used. The values of the parameters are listed in Table 2.

The char burning rate was calculated using Field's model [52]:

$$\frac{dC}{dt} = -\left(\frac{K_c K_d}{K_c + K_d}\right) P_g \pi D_p^2 \quad (3.13)$$

$$K_d = \frac{5.06 \times 10^{-7}}{D_p} \left(\frac{T_p + T_g}{2}\right)^{0.75} \quad (3.14)$$

$$K_c = A_c \exp\left(-\frac{E_c}{RT_p}\right) \quad (3.15)$$

This model is obtained under the assumption that the char burning rate is controlled by both the chemical reaction rate and the rate of diffusion of oxygen to the surface of the char particle. The values of the kinetic parameters A_c and E_c in Eq. (3.15) are 1.1×10^{-2} [$(\text{kg}/\text{m}^2 \text{s})/(\text{N}/\text{m}^2)$] and 5.0×10^4 [J/mol], respectively [3].

Table 2
Parameters for Eq. (3.12).

Reactant	A_g	E_g (J/kmol)	d (-)	f (-)	h (-)	k (-)
$\text{C}_x\text{H}_y\text{O}_z$, CH_4low , CH_4high , $\text{C}_2\text{H}_2\text{CO}$	3.09×10^8	1.67×10^8	0.5	1	0	1
	1.26×10^{10}	1.67×10^8	0	1	0.5	0.25

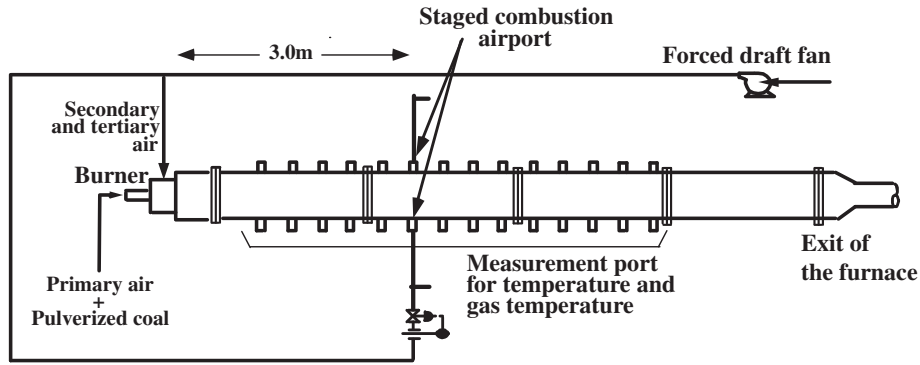


Fig. 7. Schematic of pulverized-coal-combustion test furnace.

4. Computational domain and conditions

The test furnace studied here is that at the Energy Engineering Research Laboratory of CRIEPI, in which an advanced low-NO_x burner (CI-α burner [4]) with a coal combustion capacity of about 100 kg/h is installed (Fig. 7). The furnace is a water-cooled furnace made of steel with refractory materials placed on the inside wall. The diameter and length of this furnace are 0.85 m and 8 m, respectively.

The configuration of the computational domain is shown in Fig. 8. This was designed to faithfully match the actual configuration. The computational domain is half of the furnace, and a periodic condition is applied in the azimuthal direction. Combustion air was injected into the furnace through the burner and staged combustion air ports located 3.0 m from the burner outlet. The air passing through the burner was divided into primary, secondary and tertiary air. The primary air, which carries pulverized coal, had straight motion, and the secondary and tertiary air had strong swirling motion. The swirl vane angles for the secondary and tertiary air were set at 81° and 63°, respectively, which are the optimum values for bituminous coal (these values are zero when the swirl force is zero).

The operating conditions of the furnace in the simulation were given to correspond with those in our experiment. The thermal in-

put of the coal combustion test furnace was 8.62×10^6 kJ/h (the coal feed rate for each burner was approximately 100 kg/h). The excess air ratio was 1.24, and the O₂ mole fraction at the furnace outlet was 4.0%. The staged combustion air ratio was set to 30%. The mass ratio of the pulverized coal (dry base) to the primary air was 1:2.2, and the mass ratio of secondary air to tertiary air was 1:6. The temperature of the primary air was set to 353 K, and that of the secondary and tertiary air was 598 K. Regarding the boundary condition on the wall, the temperature outside the furnace was assumed to be 308 K and thermal resistance was set to 0.04 (m² s K)/J.

The test fuel is Newlands bituminous coal, the properties of which are listed in Table 3. It was assumed that the pulverized coal particles had diameters D_p of 5, 20, 40, 60, 80 and 100 μm. The

Table 3
Coal properties for CFD simulation.

Coal	Newlands
<i>Proximate analysis (wt.%)</i>	
Moisture ^a	(3.4)
Volatile matter ^b	29.19
Fixed carbon ^b	54.76
Ash ^b	16.05
Fuel ratio (-)	1.88
<i>Ultimate analysis^b (wt.%)</i>	
C	71.70
H	4.33
N	1.43
O	6.30
Combustible sulfur	0.19
Heating value (low) ^b (MJ/kg)	28.13

^a As received basis.
^b Dry basis.

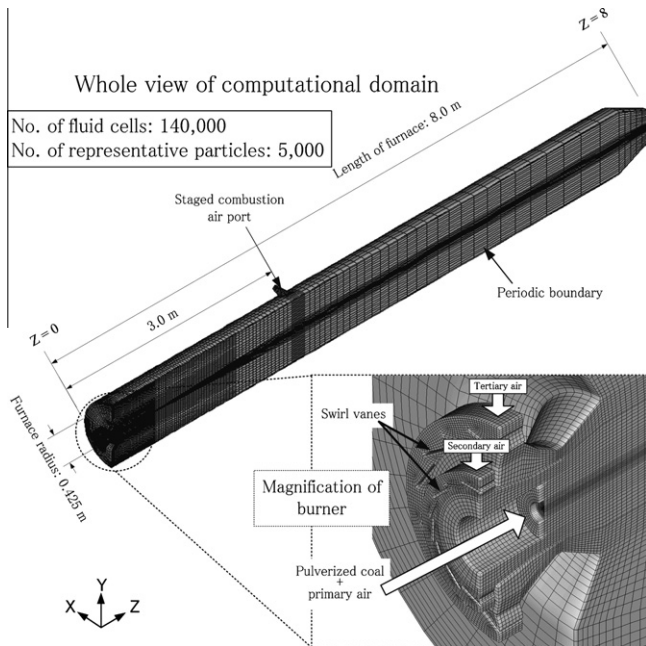


Fig. 8. Computational domain.

Table 4
Initial diameter, mass fraction and number of representative coal particles.

D_p (μm)	MF_p (-)	N_p (-)
5	6.76	320
20	26.81	1280
40	24.00	1120
60	16.25	800
80	12.20	640
100	13.98	640

Table 5
Parameters for the conventional model.

Case	Ref.	A_v (1/s)	E_v (J/kmol)	Q (-)
2	Tominaga et al. [53]	2.02×10^3	3.11×10^7	1.2
3	Solomon and Hamblen [54]	4.5×10^{13}	2.20×10^8	1.5
4	Johnson et al. [55]	1.0×10^{13}	1.8×10^8	1.8

Table 6
Parameters for the two competing reaction rate model.

Case	Ref.	α_1	α_2	A_1 (1/s)	A_2 (1/s)	E_1 (J/kmol)	E_2 (J/kmol)
5	Kobayashi et al. [25]	0.3	1	2.0×10^5	1.3×10^7	1.05×10^8	1.67×10^8
6	Cho et al. [56]	0.38	0.8	3.7×10^5	1.46×10^{13}	7.4×10^7	2.5×10^8
7	Ubhayakar et al. [57]	0.292	0.438	3.7×10^5	1.46×10^{13}	7.4×10^7	2.5×10^8

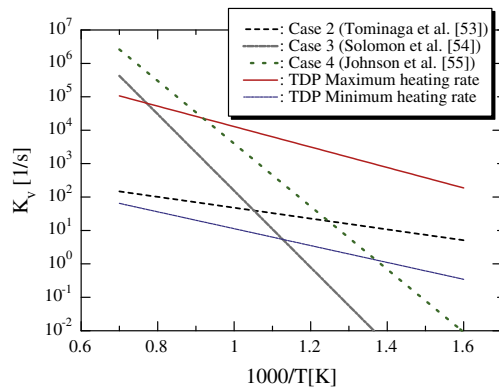


Fig. 9. K_v (in Eq. (2.1)) in an Arrhenius diagram employed by the conventional model cases.

mass fractions MF_p of coal particles and their representative particle numbers N_p are shown in Table 4. MF_p were decided to correspond with the actual particle size distribution in the experiment. The temperature and velocity of the particles at the burner inlet were equal to those of the primary air (353 K).

In this study, the simulations employing the conventional model and the two competing reaction rate model using various parameters were conducted. Rate parameters used are listed in Tables 5 and 6. Figure 9 shows K_v (in Eq. (2.1)) in an Arrhenius diagram employed in the conventional cases listed in Table 5. K_v for the maximum heating rate and the minimum heating rate in the devolatilization database employed by the TDP model are also indicated in Fig. 9. For the TDP model, K_v between the K_v for the maximum heating rate and for the minimum heating rate in the database is chosen for each coal particle depending on the particle heating rate.

5. Experimental measurement

Laser Doppler velocimetry (LDV) is used to measure the particle velocity distributions in the test furnace. Figure 10 shows a schematic of the measurement system. A commercial two-component

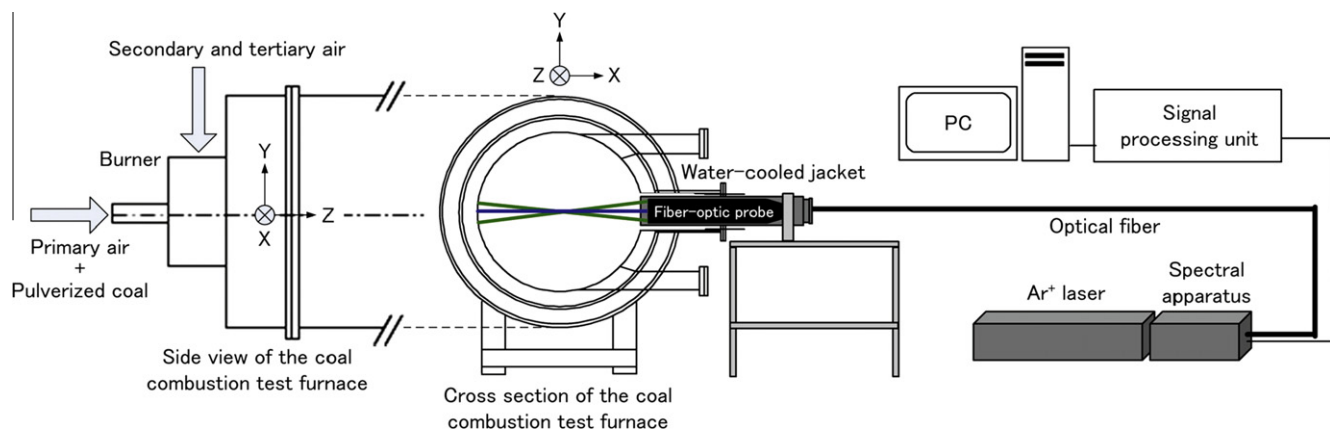


Fig. 10. Schematic diagram of particle velocity measurement system.

LDV system in a backscattering configuration and a 2 W argon-ion laser (NEC GLG3282) are used for the measurement. The system consists of a Colorburst multicolor beam separator, a Colorlink multicolor receiver, an IFA655 signal processor and a fiber-optic probe. The transmitting lens of the fiber-optic probe has a focal length of 500 mm.

The radial distributions of the mean particle velocity at the axial positions of $Z = 0.26, 0.61, 0.99$ and 1.39 in the furnace are measured by traversing the fiber-optic probe in the radial direction. To protect the optical components in the fiber-optic probe from the strong radiation of the luminous flame, the probe is set in a water-cooled jacket.

The concentration of O_2 in the furnace is measured by gas analyzer (paramagnetic method) using water cooled gas sampling probe. The gas temperature in the furnace is measured with a Pt/Pt-Rh (13%) sheath thermocouple.

6. Results and discussion

6.1. Particle behavior

Figure 11 shows the radial distributions of mean axial particle velocities at the axial distances from the burner of $Z = 0.26, 0.61, 0.99$ and 1.39 m. The dashed lines in the graphs indicate $U_z = 0$ m/s. Solid circles indicate the measurement results of the experiment, and colored solid lines indicate the predictions by simulations. Case 1 indicates the particle velocities predicted by the TDP model. Cases 2–4 indicate the particle velocities predicted by the conventional model, and devolatilization rate parameters used for these simulations are listed in Table 5. Cases 5–7 indicate the particle velocities predicted by the two competing reaction rate model, and devolatilization rate parameters are listed in Table 6. The regions where there is no line for the Case 2, 5, 7 (for example, $X > 0.11$ at $Z = 0.26$, $X < 0.2$ at $Z = 0.61$, $X < 0.8$ at $Z = 0.99$ and $X < 0.12$ at $Z = 1.39$ for Case 2) indicate the regions where no representative coal particles exist in the simulations. At the location of $Z = 0.26$, U_z near the central axis is positive for the experimental results and for the simulations other than the Case 2, whereas it is negative for the Case 2. There is no significant difference in U_z between simulations other than the Case 2. However, at the loca-

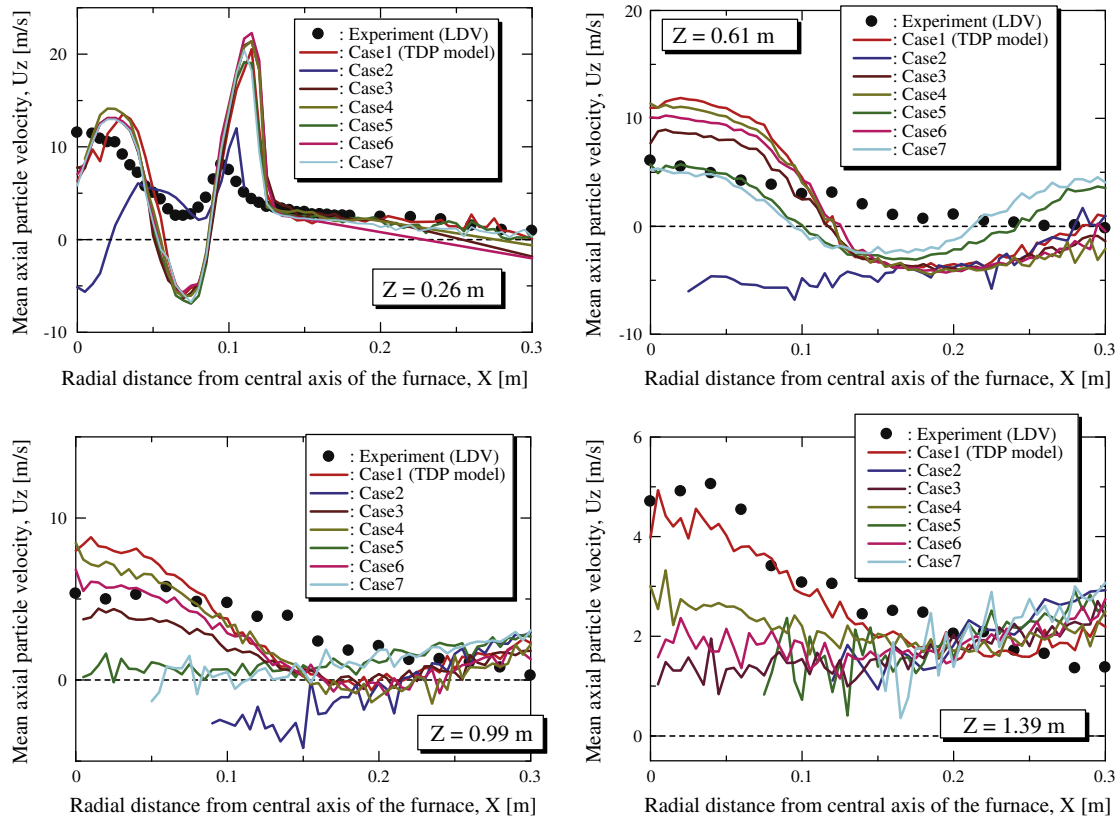


Fig. 11. Radial distributions of mean axial particle velocities.

tion of $Z = 0.61, 0.99$ and 1.39 m, there are large difference in U_z between simulation results. At the location of $Z = 0.61$, U_z for simulations other than Case 2 are positive value in the region of $X < 0.1$, while that for Case 2 is negative value. The simulations for Case 1, 3, 4 and 6 overestimate the values of U_z . For the Cases 5 and 7, the values of U_z around the central axis are in the same range with LDV measurement results. However, at the location of $Z = 0.99$ m, U_z around the central axis for the Cases 5 and 7 are almost 0 m/s, while the LDV measurement results indicate that the flow around the central axis is positive. For the Case 2, U_z is negative value in the region of $X < 0.2$. For the Cases 2 and 7, there is no particle velocity data around the central axis because of the absence of representative particle around the central axis. At the location of $Z = 1.39$ m, the values of U_z for the Case 1 (TDP model) are in better agreement with the LDV measurement results compared to that for other cases. The other cases underestimate the values of U_z around the central axis. In addition, there is no particle velocity data around the central axis for the Cases 2, 5, and 7. From all of above results, it is considered that the particle behavior predicted by the TDP model (Case 1) is in better agreement with the experiment than that predicted by other cases in this research. In what follows, detailed differences in gas velocity, particle volume fraction, volatile matter evolution rate, gas temperature and O_2 mole fraction distributions in the furnace for characteristic cases, i.e., for Cases 1, 2 and 7 are discussed.

Figure 12 shows the gas velocity vectors on the cross section at the center of the furnace for the Cases 2, 7, and 1. The colors of the vectors indicate the magnitude of the absolute velocity. It is observed that the gas flow patterns predicted by the Case 2 (a) and Case 1 (c) are considerably different. The gas flow velocity on the central axis of the furnace for the Case 1 is positive throughout the furnace, while there is a large region where the gas velocity on the central axis of the furnace is negative near the burner exit

for the Case 2. For the Case 7, the positive flow near the burner exit is stronger than that for Case 2. However, there is negative flow on the central axis in the region around $X = 1.0$. These large differences in the gas flow pattern cause the difference in the particle velocity distributions shown in Fig. 11. For the Case 2, the coal particles, which are supplied from the center of the burner with the primary air, cannot penetrate the strong reverse flow region around the central axis of the furnace. For the Case 1, on the other hand, most of the particles advance straight with the positive flow around the central axis. This is the reason why the axial distributions of the particle velocity are markedly different between the simulations as observed in Fig. 11.

Figures 13 and 14 show the particle volume fraction on the cross section at the center of the furnace and the distributions of the coal particles, respectively. The colors of the particle in Fig. 14 indicate the particle temperature. The difference in the particle volume fraction is marked in Fig. 13. For the Case 2, almost no particles exist around the central axis in the downstream region of $Z > 0.3$, and a high particle volume fraction is observed near the furnace wall. Most of the particles are blown to the region near the furnace sidewall due to the strong negative flow on the central axis as shown in Fig. 12a. Consequently, the particle volume fraction near the furnace sidewall is high, while that near the central axis is low in the downstream region of $Z > 0.3$. In the region near the burner exit ($Z < 0.3$), the particle volume fraction around the central axis is high and there is almost no particle with high temperature in this region as observed in Fig. 14a. For the Case 7, almost no particles exist around the central axis in the downstream region of $Z > 0.9$ as shown in Fig. 13b. This is caused by the fact most of the particles are blown to the region near the furnace sidewall due to the negative flow in the region around $Z = 1.0$ as observed in Fig. 12b, same as Case 2. For the Case 1, on the other hand, a high particle volume fraction is observed around the

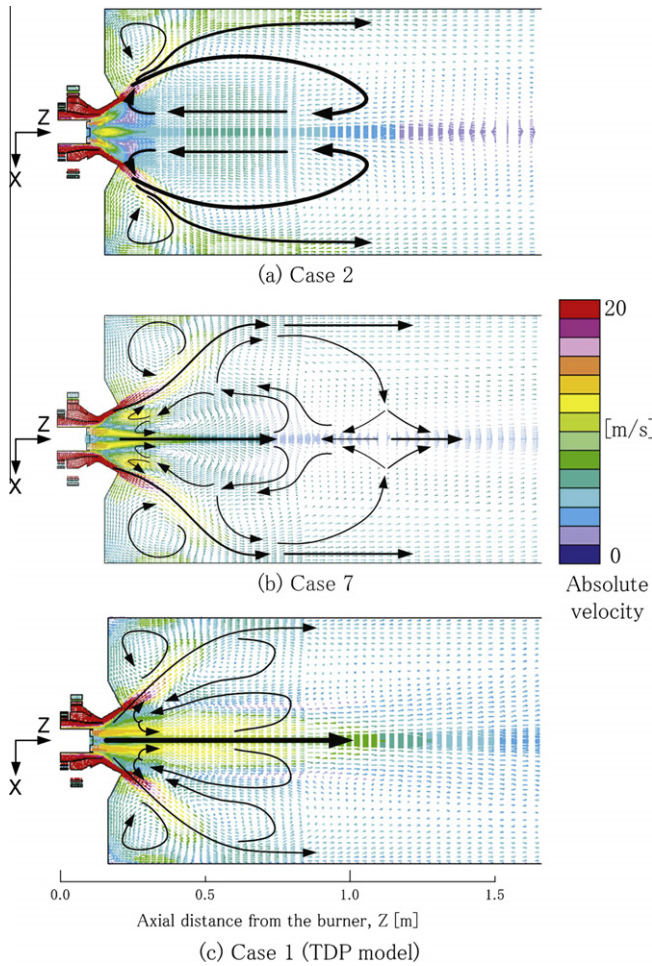


Fig. 12. Gas velocity vectors on the cross section at the center of the furnace.

central axis throughout the region in Fig. 13c. It should also be noted that there are some particles with high temperature in the region near the burner exit as observed in Fig. 14c. This particle behavior for the Case 1 is consistent with the photograph of the flame taken during the experiment.

Figure 15 shows the flame photograph obtained during the experiment. A luminous flame with a columnar shape is observed in the region around the central axis of the furnace. The luminous flame begins from vicinity of the burner exit. In the region where the luminous flame is observed, it is considered that there must be high-temperature coal particles with sufficiently high particle volume fraction to be observed as the luminous flame. As observed in Figures 13 and 14c, for the Case 1, the high-temperature particles with a high particle volume fraction exist in the region around the central axis where the luminous flame is observed in the experiment. For the Case 2, on the other hand, they exist only in the region near the furnace sidewall where the luminous flame is not observed in the experiment. For the Case 7, there is a region where high-temperature coal particles are observed around the central axis. However, the region is short and high-temperature coal particles are also observed near the furnace sidewall where the luminous flame is not observed in the experiment.

Overall, it is apparent that the Case 1 captures the observed behavior of the coal particles better than the other cases.

6.2. Devolatilization behavior

Figure 16 shows the distributions of the volatile matter evolution rate on the cross section at the center of the furnace. The peak

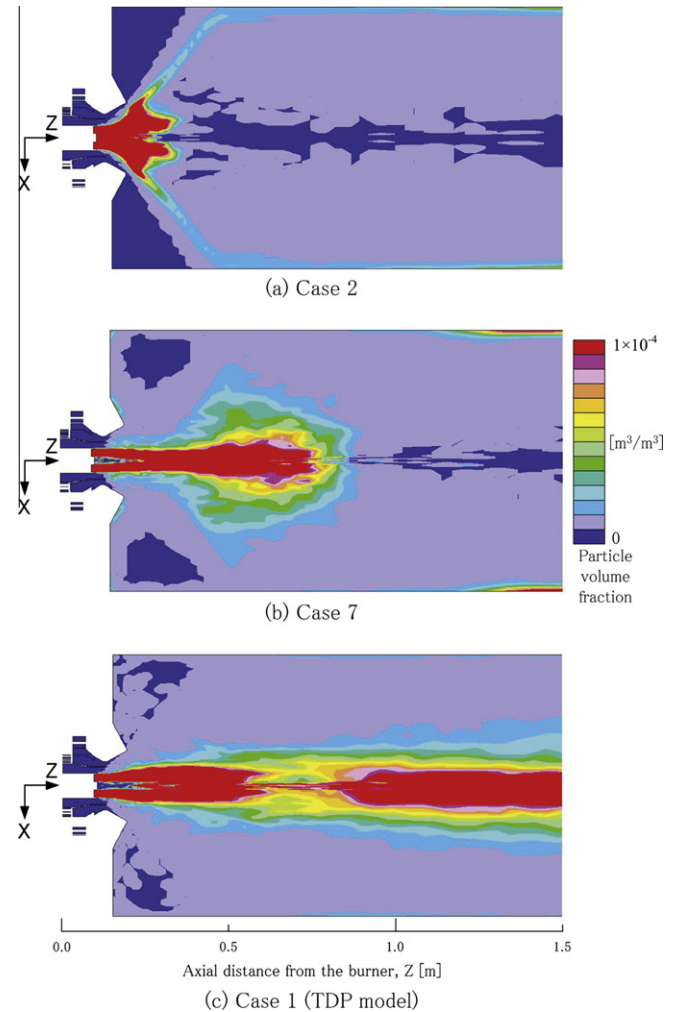
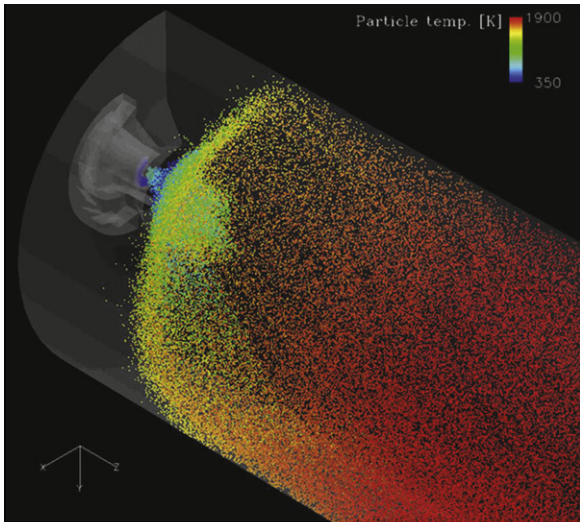


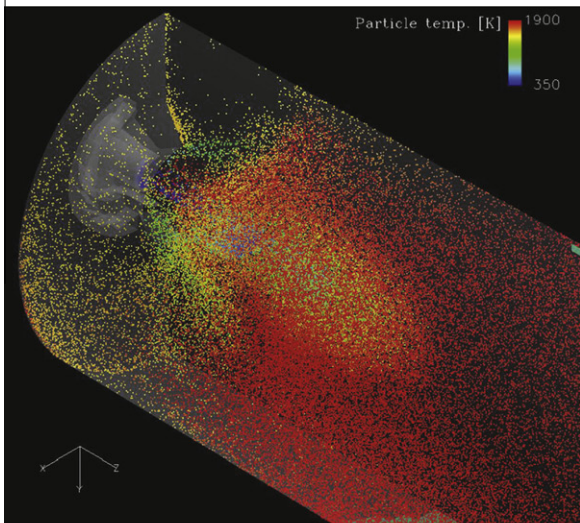
Fig. 13. Distributions of particle volume fraction on the cross section at the center of the furnace.

value of the volatile matter evolution rate for the Case 1 is over two times larger than that for the Cases 2 and 7. This is caused by the fact that the coal particle heating rate in this study is relatively high.

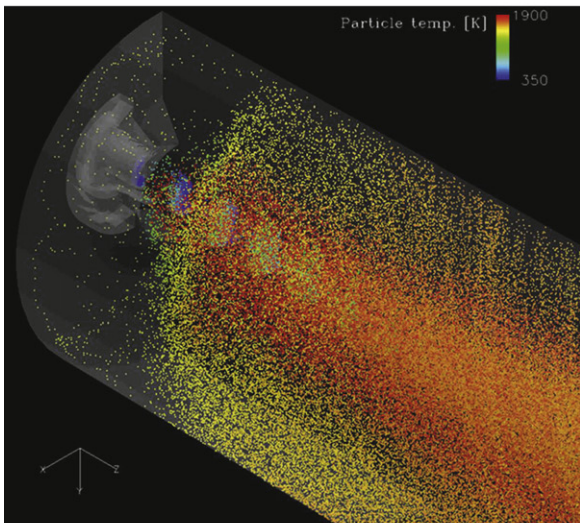
Figure 17 shows the probability of selection of each temperature history in the devolatilization database when particle temperature histories calculated in the CFD iteration are compared with temperature histories in the database (Fig. 6) for the TDP model. The horizontal axis indicates the particle heating rate of each temperature history in the devolatilization database. The probabilities of selection of the temperature histories were calculated by averaging the number of selections during 1000 iterations after the convergence of the CFD calculation was achieved. It is found that the heating rates of most of the particles are in the range of 10^4 – 10^6 K/s. In the TDP model, A_v and E_v giving a high devolatilization rate, and a high value of $m_{v,ola}$ for the particle are set for the next iteration when a temperature history with a high heating rate is selected from the devolatilization database. Consequently, the volatile matter evolution rate in the region near the burner exit for the TDP model is higher than that for the conventional model, as can be observed in Fig. 16. The larger amount of volatile matter evolved from the coal particles causes greater gas expansion due to the increase in the gas volume and the combustion of volatile matter. In other words, the gas expansion due to the volatile matter evolution and its combustion in the region near the burner exit for the TDP model



(a) Case 2



(b) Case 7



(c) Case 1 (TDP model)

Fig. 14. Distributions of coal particles with particle temperature.

is greater than those for the conventional model. This is the reason why the gas flow patterns predicted by the TDP model and



Fig. 15. Flame photograph obtained during the experiment.

other cases are markedly different in Fig. 12. Because of the large gas expansion owing to the high evolution rate of volatile matter, the penetrating force of the straight flow from the primary air, which is supplied with the pulverized coal particles from the center of the burner, is strong for the Case 1. Due to the strong penetrating force, the straight flow from the primary air can overcome the recirculation flow induced by the secondary and tertiary air, which have strong swirling motion. Consequently, the gas flow velocity on the central axis of the furnace for the TDP model is positive throughout the furnace.

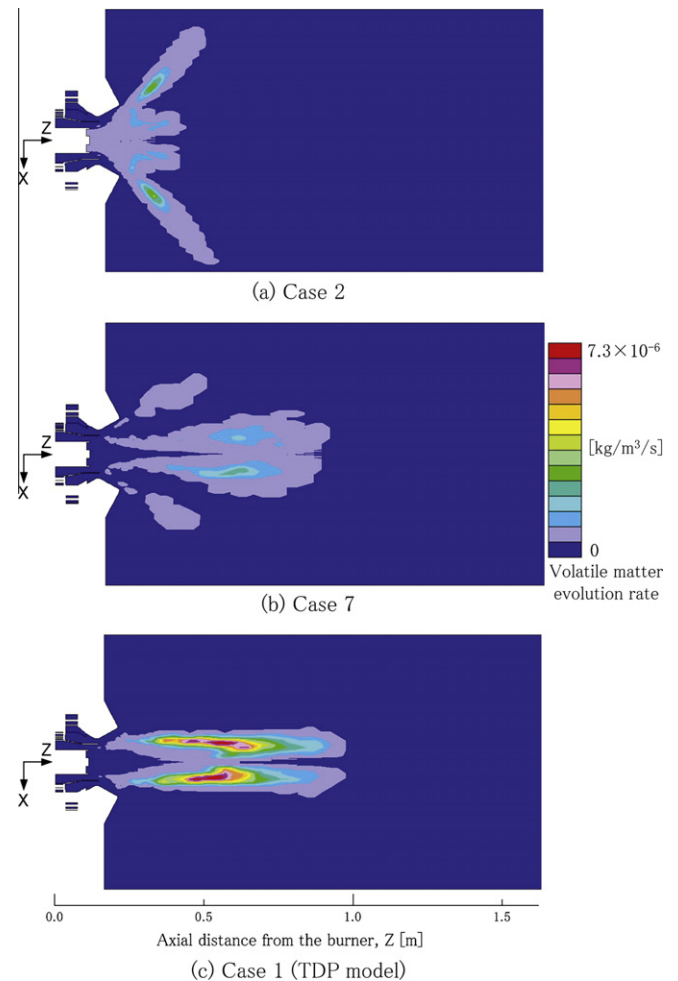


Fig. 16. Distributions of volatile matter evolution rate on the cross section at the center of the furnace.

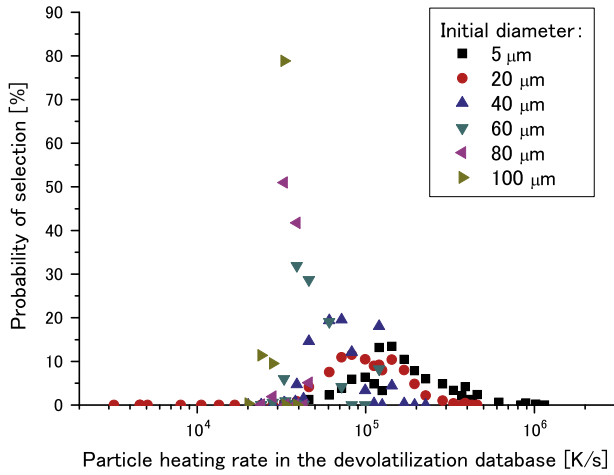


Fig. 17. Probability of selection for each particle heating rate of temperature history in the devolatilization database during the selection process (Fig. 6).

For the Case 2, on the other hand, the straight flow from the primary air cannot overcome the recirculation flow induced by the secondary and tertiary air, because the penetrating force of the straight flow from the primary air is weak due to the low evolution rate of volatile matter. It should also be noted that the large variations in particle heating rate depending on the initial diameter are observed in Fig. 17. It is found that the smaller the initial diameter is, the higher the heating rate of the selected temperature history is.

6.3. Gas temperature and O₂ mole fraction distributions

Figure 18 shows the distributions of the predicted gas temperature and the value indicated by the thermocouple in the experiment on the cross section at the center of the furnace. The radiative heat loss from the thermocouple was not corrected because of the difficulty of the estimating the furnace wall temperature. For the Case 2, the maximum temperature is observed in the region near the furnace wall. This is caused by the fact that the

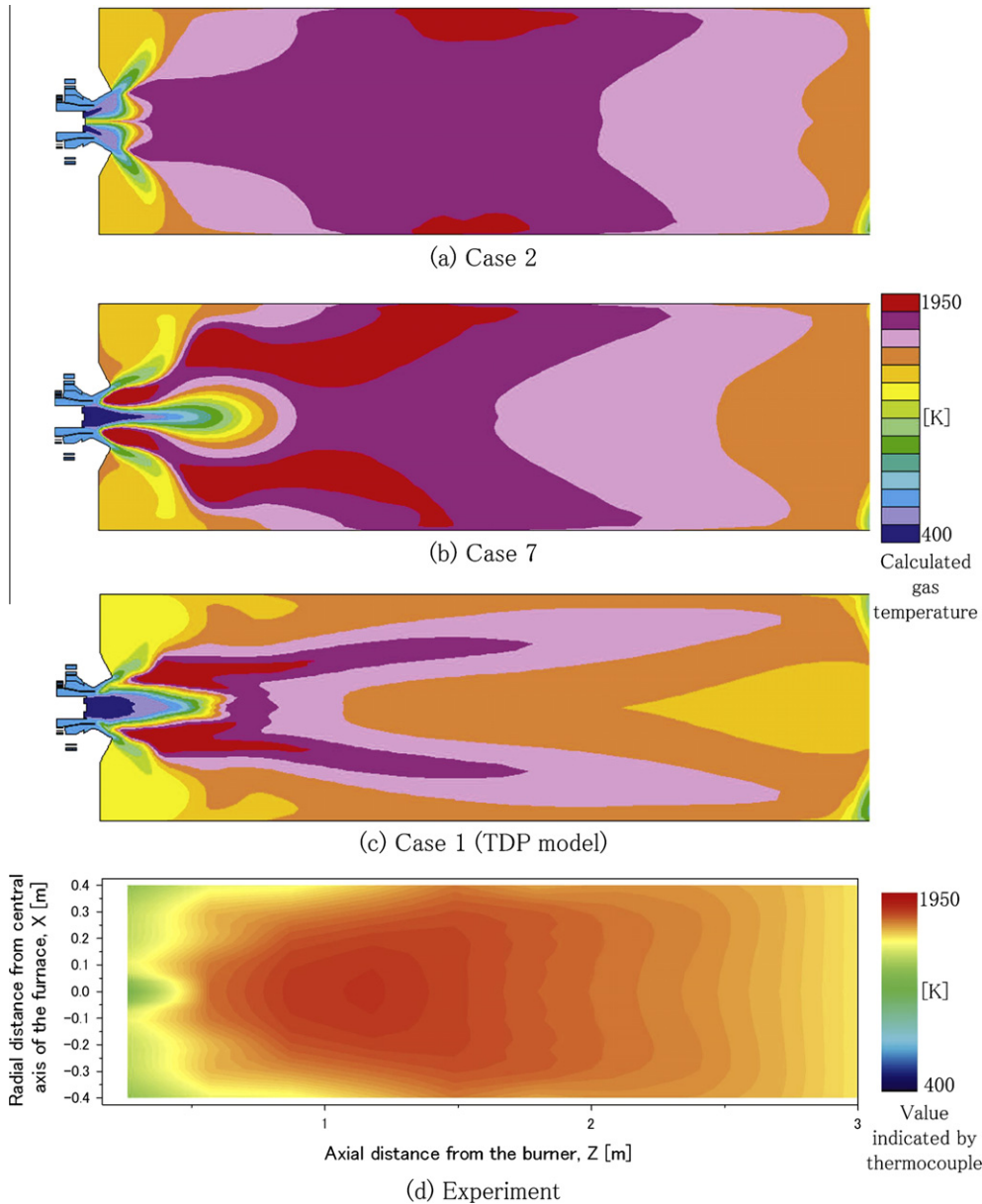


Fig. 18. Distributions of the predicted gas temperature and the value indicated by the thermocouple in the experiment on the cross section at the center of the furnace.

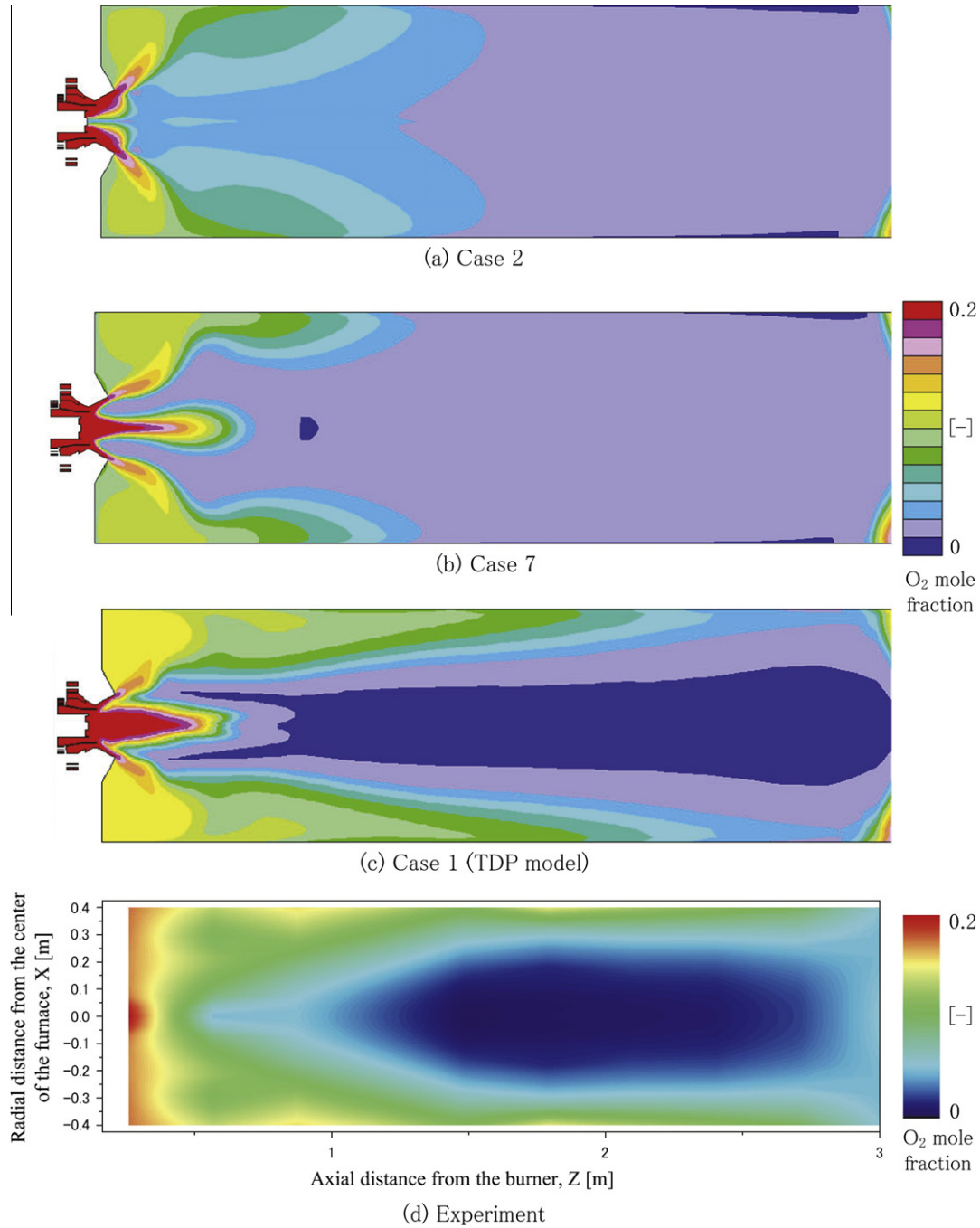


Fig. 19. Distributions of the predicted O₂ mole fraction and that measured in the experiment on the cross section at the center of the furnace.

most of the char combustion reaction takes place near the furnace wall because most of the coal particles are blown to the region near the furnace sidewall for the Case 2, as previously explained. For the Case 7, the maximum temperature is observed near the burner exit and in the region near the furnace wall. For the Case 1, on the other hand, the maximum temperature is observed in the region near the central axis of the furnace, and this tendency is consistent with that observed in the experiment.

Figure 19 shows the distributions of the predicted O₂ mole fraction and that measured in the experiment on the cross section at the center of the furnace. For the Cases 2 and 7, the gradient of the O₂ mole fraction in the radial direction is relatively small and the O₂ mole fraction is low regardless of the radial position,

in the downstream region of $Z > 1.5$ m. For the Case 1, on the other hand, the O₂ mole fraction in the region near the central axis is nearly 0, and the O₂ mole fraction increases as the radial distance from the central axis increases in the downstream region of $Z > 1.0$ m. This tendency is consistent with that observed in the experiment.

In this study, it was found that the particle behavior predicted by the TDP model is in better agreement with the experiment than that predicted by other cases in this research. Even for the conventional model or the two competing reaction rate model, it may be possible to obtain particle velocity distributions similar to that for the TDP model by adjusting the devolatilization parameters. However, a trial-and-error method is required to obtain appropriate

values for the devolatilization parameters because the coal particle heating rates, which depend strongly on the combustion field, cannot easily be known in advance. Furthermore, the influence of variations in coal particle heating rate as observed in Fig. 17 on the devolatilization behavior cannot be taken into account by the conventional model. Even though the two competing reaction rate model can consider the effect of coal particle heating rate, it is found that inappropriate devolatilization parameters might cause the large error in the particle behavior prediction.

Although the particle velocity distributions predicted by the TDP model was in better agreement with the experiment than that predicted by the other models, there are some discrepancies between the TDP model and the experiment. For instance, in Fig. 11, the discrepancies in the particle velocity distributions between the simulation employing the TDP model and the experiment at $Z = 0.26$ and 0.61 m are relatively large, while the discrepancies at $Z = 0.99$ and 1.39 m are relatively small. This is considered to be due to the low accuracy of the prediction of turbulent mixing for the RNG $k-\epsilon$ model. Watanabe et al. [58] performed a numerical simulation of swirling cold-flows in the same test furnace as that used in this study and found that the accuracy of the prediction of the characteristics of the recirculation flow by the $k-\epsilon$ model is lower than that obtained by the large-eddy simulation (LES). Therefore, the coupling of the TDP model with the LES is our future work.

7. Conclusions

In this study, numerical simulations of a pulverized coal combustion field formed by an industrial low- NO_x burner in a 100 kg-coal/h test furnace were performed employing the TDP model, and its validity was examined. The predicted characteristics of the pulverized coal combustion field are compared with those employing the conventional model and the two competing reaction rate model.

It was found that the particle behavior predicted by the TDP model was in better agreement with the experiment than that predicted by the other models. The differences in the coal particle behavior were caused by the difference in the gas flow patterns. The gas flow patterns predicted by the TDP model and the conventional model with the some rate parameters were markedly different. This large difference was caused by the fact that the penetrating force of the flow from the primary air port was strong for the TDP model due to the strong gas expansion effect. The large gas expansion effect for the TDP model is caused by the high volatile matter evolution rate from the coal particles with a high particle-heating rate. Consequently, the straight flow from the primary air port is dominant for the TDP model, while the large recirculation flow induced by the swirling flow is dominant for the conventional model. The inappropriate prediction of devolatilization behavior by the conventional model observed in this study is attributed to the fact that the devolatilization parameters are given based on the empirical information obtained from different combustion fields, whereas those for the TDP model are selected for individual particle based on the information obtained from the combustion field of interest. Even though it is considered that it is possible to obtain particle velocity distributions similar to that for the TDP model by adjusting the devolatilization parameters for the conventional model or the two competing reaction rate model, a trial-and-error method is required to obtain appropriate values for the devolatilization parameters. Furthermore, the variations of devolatilization parameters depending on the coal particle heating rate cannot be considered in the conventional model. By employing the TDP model, appropriate devolatilization parameters are automatically set to particles depending on the particle heating rate.

References

- [1] M.M. Baum, P.J. Street, *Combust. Sci. Technol.* 3 (1971) 231–243.
- [2] International Energy Outlook 2007; Energy Information Administration, Washington, DC, 2007, pp. 49–60.
- [3] N. Hashimoto, R. Kurose, H. Tsuji, H. Shirai, *Energy Fuels* 21 (2007) 1950–1958.
- [4] R. Kurose, H. Makino, A. Suzuki, *Fuel* 83 (2004) 693–703.
- [5] R. Kurose, M. Ikeda, H. Makino, *Fuel* 80 (2001) 1447–1455.
- [6] R. Kurose, H. Tsuji, H. Makino, *Fuel* 80 (2001) 1457–1465.
- [7] R. Kurose, H. Watanabe, H. Makino, *KONA Powder Part. J.* 27 (2009) 144–156.
- [8] T. Asotani, T. Yamashita, H. Tominaga, Y. Uesugi, Y. Itaya, S. Mori, *Fuel* 87 (2008) 482–490.
- [9] M. Kumar, S.G. Sahu, *Energy Fuels* 21 (2007) 3189–3193.
- [10] R.I. Backreedy, L.M. Fletcher, L. Ma, M. Pourkashanian, A. Williams, *Combust. Sci. Technol.* 178 (2006) 763–787.
- [11] L.X. Zhou, L. Li, R.X. Li, J. Zhang, *Powder Technol.* 125 (2002) 226–233.
- [12] J. Pallares, I. Arauzo, L.I. Diez, *Fuel* 84 (2005) 2364–2371.
- [13] R.I. Backreedy, J.M. Jones, L. Ma, M. Pourkashanian, A. Williams, A. Arenillas, B. Arias, J.J. Pis, F. Rubiera, *Fuel* 84 (2005) 2196–2203.
- [14] A. Bosoaga, N. Panoiu, L. Mihaescu, R.I. Backreedy, L. Ma, M. Pourkashanian, A. Williams, *Fuel* 85 (2006) 1591–1598.
- [15] C.M. Lee, K.A. Davis, M.P. Heap, E. Eddings, A. Sarofim, *Proc. Combust. Inst.* 28 (2000) 2375–2381.
- [16] J.R. Valentine, H.-S. Shim, K.A. Davis, S.-I. Seo, T.-H. Kim, *Energy Fuels* 21 (2007) 242–249.
- [17] R.H. Schlosberg, *Chemistry of Coal Conversion*, Plenum Press, New York, 1985, pp. 131–138.
- [18] J.R. Gibbins, C.K. Man, K.J. Pendlebury, *Combust. Sci. Technol.* 93 (1993) 349–361.
- [19] S. Badzioch, P.G.W. Hawksley, *Ind. Eng. Chem. Process Des. Dev.* 9 (1970) 521–530.
- [20] M. Azhakesan, K.D. Bartle, P.L. Murdoch, J.M. Taylor, A. Williams, *Fuel* 70 (1991) 322–328.
- [21] H.-Y. Cai, A.J. Guell, I.N. Chatzakis, J.-Y. Lim, D.R. Dugwell, R. Kandiyoti, *Fuel* 75 (1996) 15–24.
- [22] A.J. Güell, H.-Y. Cai, D.R. Dugwell, R. Kandiyoti, *Fuel Process. Technol.* 36 (1993) 259–265.
- [23] C.-Z. Li, K.D. Bartle, R. Kandiyoti, *Fuel* 72 (1993) 3–11.
- [24] J. Yu, J.A. Lucas, T.F. Wall, *Prog. Energy Combust.* 33 (2007) 135–170.
- [25] H. Kobayashi, J.B. Howard, A.F. Sarofim, *Proc. Combust. Inst.* 16 (1977) 411–425.
- [26] S.-W. Du, W.-H. Chen, *Int. Commun. Heat Mass Transfer* 33 (2006) 327–334.
- [27] T.H. Fletcher, A.R. Kerstein, R.J. Pugmire, D.M. Grant, *Energy Fuels* 4 (1990) 54–60.
- [28] T.H. Fletcher, A.R. Kerstein, R.J. Pugmire, M.S. Solum, D.M. Grant, *Energy Fuels* 6 (1992) 414–431.
- [29] P.R. Solomon, M.A. Serio, E.M. Suuberg, *Prog. Energy Combust. Sci.* 18 (1992) 133–220.
- [30] S. Niksa, *Combust. Flame* 100 (1995) 384–394.
- [31] S. Niksa, A.R. Kerstein, *Energy Fuels* 5 (1991) 647–665.
- [32] S. Niksa, *Energy Fuels* 5 (1991) 665–673.
- [33] S. Niksa, *Energy Fuels* 5 (1991) 673–683.
- [34] S. Niksa, *Energy Fuels* 8 (1994) 659–670.
- [35] S. Niksa, *Energy Fuels* 8 (1994) 671–679.
- [36] S. Niksa, *Energy Fuels* 9 (1995) 467–478.
- [37] S. Niksa, *Energy Fuels* 10 (1996) 173–187.
- [38] D. Genetti, T.H. Fletcher, R.J. Pugmire, *Energy Fuels* 13 (1999) 60–68.
- [39] PC Coal Lab Version 3.2 User Guide and Tutorial, Niksa Energy Associates, 2004.
- [40] V. Yakhot, S.A. Orszag, *J. Sci. Comput.* 1 (1986) 3–51.
- [41] V. Yakhot, S.A. Orszag, S. Thangam, T.B. Gatski, C.G. Speziale, *Phys. Fluids* 4 (1992) 1510–1520.
- [42] B.E. Launder, D.B. Spalding, *Comput. Methods Appl. Mech. Eng.* 3 (1974) 269–289.
- [43] A.M. Eaton, L.D. Smoot, S.C. Hill, C.N. Eatough, *Prog. Energy Combust.* 25 (1999) 387–436.
- [44] R.I. Issa, *Comp. Phys.* 62 (1986) 40–65.
- [45] R.I. Issa, A.D. Gosman, A.P. Watkins, *J. Comput. Phys.* 62 (1986) 66–82.
- [46] A.D. Gosman, E. Ioannides, *AIAA paper* 1981, No. 81-0323.
- [47] R. Siegel, J. Howell, *Thermal Radiation Heat Transfer*, fourth ed., Taylor & Francis, New York, 2002, pp. 681–695.
- [48] C.T. Crowe, M.P. Sharma, D.E. Stock, *Trans. ASME J. Fluids Eng.* 99 (1977) 325–332.
- [49] B.F. Magnussen, B.H. Hjertager, *Proc. Combust. Inst.* 16 (1976) 719–729.
- [50] R.B. Pember, L.H. Howell, J.B. Bell, P. Colella, W.Y. Crutchfield, W.A. Fiveland, J.P. Jessee, *Combust. Sci. Technol.* 140 (1998) 123–168.
- [51] M.A. Field, *Combust. Flame* 13 (1969) 237–252.
- [52] H. Tominaga, M. Harada, T. Ando, Y. Suzuki, *J. NIRE* 6 (1997) 333–343. in Japanese.
- [53] P.R. Solomon, D.G. Hamblen, *Prog. Energy Combust.* 9 (1983) 323–361.
- [54] G.R. Johnson, P. Murdoch, A. Williams, *Fuel* 67 (1988) 832–834.
- [55] C.P. Cho, S. Jo, H.Y. Kim, S.S. Yoon, *Numer. Heat Transfer, Part A: Appl.* 52 (2007) 1101–1122.
- [56] S.K. Ubhayakar, D.B. Stickler, C.W. von Rosenberg, R.E. Gannon, *Proc. Combust. Inst.* 16 (1976) 427–436.
- [57] H. Watanabe, R. Kurose, S. Komori, *J. Environ. Eng.* 4 (2009) 1–11.